Available online at www.sciencedirect.com

jmr&t Journal of Materials Research and Technology

journal homepage: www.elsevier.com/locate/jmrt

Original Article

Viscoplastic and temperature behavior of Zn–Cu–Ti alloy sheets: experiments, characterization, and modeling

Francisco Alister [a,*], *Diego Celentano* [a], *Javier Signorelli* [b], *Pierre-Olivier Bouchard* [c], *Daniel Pino Muñoz* [c], *Marcela Cruchaga* [d]

[a] *Department of Mechanical and Metallurgical Engineering, Pontificia Universidad Católica de Chile, Avenida Vicuña Mackenna 4860, Macul, Chile*

[b] *Instituto de Física Rosario (UNR-CONICET), Ocampo y Esmeralda, Rosario, Santa Fe, Argentina*

[c] *MINES ParisTech, PSL Research University, CEMEF-Centre de Mise en Forme des Matériaux, CNRS UMR 7635, CS 10207 Rue Claude Daunesse, 06904, Sophia Antipolis Cedex, France*

[d] *Department of Mechanical Engineering, Universidad de Santiago de Chile, Avenida Bernardo O'Higgins 3363, Santiago, Chile*

ARTICLE INFO

Article history:
Received 9 April 2021
Accepted 29 September 2021
Available online 5 October 2021

Keywords:
Zinc alloys
Zn–Cu–Ti
CPB-06
Johnson–Cook
Strain-rate
Temperature influence

ABSTRACT

It has been experimentally observed that the Zn–Cu–Ti zinc alloy shows a strong influence of strain rate and temperature on its plastic behavior. A significant change in the material response is seen with relatively small strain rate variations or temperature. In this work, these effects are addressed through the Cazacu–Plunket–Barlat 2006 (CPB-2006) yield criterion and the Johnson–Cook hardening law. The tests were carried out over the three main directions: rolling, diagonal, and transversal. Three strain rate conditions (0.002, 0.02, and 0.2 s^{-1}) and three temperatures (20, 60, and 80 °C) were tested. Although the experimental results exhibit a significant influence of the strain rate and temperature on stress–strain curves for all tested directions, such two variables do not practically affect the Lankford coefficients. The proposed model calibration procedure is found to describe the material responses properly under the studied conditions.

1. Introduction

The use of Zn–Ti–Cu alloys has been especially pulled by construction and architecture applications. These areas take advantage of the excellent corrosion resistance and long-lasting surface finish from zinc, while titanium increases its mechanical resistance and copper improves its malleability. These features allow skin-type creations in vanguard projects. Besides, its cost is considerably lower than other materials such as titanium. Despite its wide range of applications and advantages, there is a reduced number of research works on these types of alloys. These studies on Hexagonal Close-Packed focuses on metals like titanium, magnesium, or zirconium [1–7].

* Corresponding author.
E-mail address: fjaliste@uc.cl (F. Alister).

https://doi.org/10.1016/j.jmrt.2021.09.132

The rolling process in zinc alloy production generates significant texture changes inducing a high dependency with the material orientation, increasing the difficulty of describing the plastic behavior of this material. In particular, rolled zinc alloys exhibit Lankford coefficients below 1 and significantly different between directions. Furthermore, the hardening has a significant and consistent rise for the rolling to the transverse direction. Studies on zinc alloys have focused mainly on determining its formability under different loading paths and the evolution of its texture. A detailed description of zinc alloys anisotropy and the influence of the rolling process can be found in the works of Phillippe et al., Faur and Cosmeleață, Pantazopoulos et al., Milesi et al., Schlosser et al., and Alister et al. [8–16]. From a different point of view, all these works present experimental results that evidence the marked anisotropy of rolled zinc alloys in terms of hardening and plastic strain related to the direction of the samples, performing a material characterization under quasi-static and isothermal conditions.

The anisotropy behavior of zinc alloys has been studied using crystal models and phenomenological frameworks. For example, Cauvin, Schwindt, and Borodachenkova [17–19] use the viscoplastic self-consistent (VPSC) approach to describe the plastic behavior of zinc alloys based on the texture evolution under quasi-static and isothermal conditions. From a phenomenological view, the research of Jansen and Milesi [14,20–25] focuses on modeling the behavior of zinc alloys in different forming processes. In their works, Jansen and Milesi developed the "Fiber Vector" concept to determine zinc formability via the Forming Limit Diagram (FLD). The "Fiber Vector" defines the Eigen stress and strains through angle-dependent parameters related to Hill 48 anisotropy coefficients to describe the anisotropic behavior of metal sheets, mainly applied on Zn–Cu–Ti alloys. The work of Milesi et al. is extended in Alister et al. [15] using the CPB-06 yield function to face the numerical estimation of zinc alloy behavior. However, all these works are established under a strain-rate independent and isothermal framework.

The material response under different forming conditions has been reported in Leonard et al. [16] and Milesi et al. [26], showing that similar zinc alloys present high strain rate sensitivity. Furthermore [8,11,27], studied Zn–Cu and Zn–Cu–Ti alloy's response under different temperature conditions and its effect on material formability showing this condition's influence. It is worth mentioning that the high sensitivity to temperature and strain rate makes self-heating effects significant in the material behavior. Milesi et al. studied the effect of self-heating phenomena in [27], where the plastic work was analyzed using numerical and experimental tests. Although these researches show the strong influence of strain rate and temperature in the material behavior, no one of them analyzes both factors in the numerical modeling of Zinc alloys.

In this work, using the CPB-06 yield function [28,29] and the Johnson–Cook hardening law [30], the anisotropy of a Zn–Ti–Cu alloy is experimentally characterized and modeled to establish a material description involving strain-rate and temperature-dependent effects as a framework for further numerical simulations in different forming scenarios.

2. Material and methods

2.1. Material

The material used in this work is a sheet of Zn–Cu–Ti alloy named Zn-20, with a nominal thickness of 0.65 mm. All test samples were cut along the rolling direction RD (0°), diagonal direction DD (45°), and transversal direction TD (90°). RD and TD are aligned with the x-and y-axis of the reference system. As a result, the z-axis is the out-of-plane component.

The uniaxial tensile stress–strain curves show no significant difference for all samples' elasticity moduli (E). The E value was established to 99.0 GPa [31]. No variation of E related to temperature or strain rate was considered in this study. The Poisson ratio is 0.24 [32]. The yield stress σ_{yp} was obtained with the 0.002 strain offset.

The Lankford coefficients were computed from the DIC images over the gauge area from the yield point to the maximum stress in the true-stress strain curve. Leonard et al. [33] and Alister et al. [15] showed that a homogeneous state could be considered until such point for the Zn-20 (Onset of Necking). Mean values for R of 0.24, 0.33, and 0.73 for RD, DD, and TD, respectively, were found. There is no significant difference for R-value in the same direction at different testing conditions.

2.2. Experimental procedure

Uniaxial tensile tests were carried out with an Instron 5967 Universal Testing machine, equipped with a 30 kN load cell and an isolated heating chamber for temperature dependence experiments. Two repetitions per direction (RD, DD, and TD) and condition (strain rate and temperature) were performed for a total of 30 experiments. The sample shape was defined according to ASTM E8-8M. All specimens were cut along the three main directions described above (RD, DD,

Table 1 – Experiments performed.

Condition	Direction	Qty.	Strain rate s^{-1}	Temperature °C
Low strain-rate low temperature (Control)	RD	2	0.002	20
	DD	2	0.002	20
	TD	2	0.002	20
Medium strain-rate low temperature (0.02 s^{-1})	RD	2	0.02	20
	DD	2	0.02	20
	TD	2	0.02	20
High strain-rate low temperature (0.2 s^{-1})	RD	2	0.2	20
	DD	2	0.2	20
	TD	2	0.2	20
Low strain-rate medium temperature (60 °C)	RD	2	0.002	60
	DD	2	0.002	60
	TD	2	0.002	60
Low strain-rate high temperature (80 °C)	RD	2	0.002	80
	DD	2	0.002	80
	TD	2	0.002	80

and TD). All experiments performed are detailed in Table 1. Fig. 1 shows the experimental setups for the strain-rate and temperature experiments together with the speckled tensile samples used.

The displacements and later strain field computation were obtained with a 3D Digital Image Correlation (3D DIC) system VIC 3D 8 by Correlated Solutions. Two pairs of high-resolution cameras with 4.0 Megapixels resolution at 10 frames per second (fps) were used (Point Grey Grasshopper for strain rate and Allied Technologies Pike for temperature dependency).

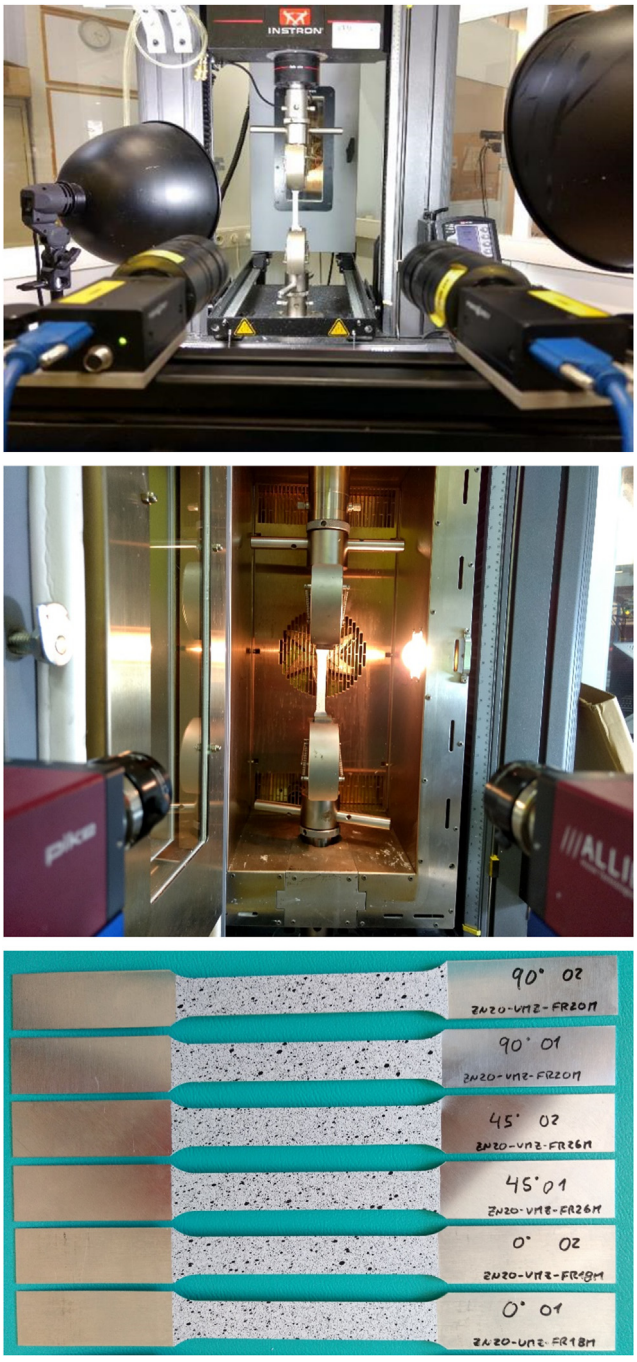

Fig. 1 – Top: Strain-rate setup. Middle: The heating chamber for variable temperature experiments. Bottom: ASTM E8 Tensile test samples with speckle pattern.

The post-process parameter to obtain the strain fields was set to 19 and 3 pixels for the grid and step size. The load data was recorded for each time step and frame using an analog–digital converter provided by National Instruments [15].

An isolated chamber with controlled temperature was used for the variable temperature tests containing the grips and samples. At the same time, the samples were stored inside the chamber to standardize their temperature to the test conditions. Three minutes of holding time were used for each test to stabilize the chamber temperature after mounting the new sample.

2.3. *Constitutive model*

The constitutive model adopted in this work modifies that already reported in [15,28,29,34,35]. The model considers an elastic and viscoplastic material model under an associated flow rule. Besides, the strain rate and temperature dependencies are driven through the use of a Johnson–Cook hardening model.

The constitutive model is implemented in an in-house finite element code with a radial-return scheme based on the Newton–Raphson iterative method [36].

2.3.1. *Yield function*

The CPB-06 yield criterion chosen to describe the material behavior is written as [28–30,34]:

$$F_{\left(\boldsymbol{\sigma},\bar{\varepsilon}_p,\dot{\bar{\varepsilon}}_p,T^\circ\right)} = \bar{\sigma}_{(\boldsymbol{\sigma})} - Y_{\left(\bar{\varepsilon}_p,\dot{\bar{\varepsilon}}_p,T^\circ\right)} = 0 \tag{1}$$

where $\bar{\sigma}$ is the equivalent stress, $\boldsymbol{\sigma}$ is the Cauchy stress tensor (in a general Cartesian reference system), and Y is the isotropic strain rate and temperature-dependent hardening stress for which $\bar{\varepsilon}_p$ is the equivalent plastic strain, $\dot{\bar{\varepsilon}}_p$ is its strain rate, and T° is the material temperature. The equivalent stress is given by:

$$\bar{\sigma}_{(\boldsymbol{\sigma})} = \left(\frac{f}{B_{0^\circ}}\right)^{\frac{1}{a}} \tag{2}$$

where f and B_{0° are defined as:

$$f = \left(|\Sigma_1| - k\Sigma_1\right)^a + \left(|\Sigma_2| - k\Sigma_2\right)^a + \left(|\Sigma_3| - k\Sigma_3\right)^a \tag{3}$$

$$B_{0^\circ} = \left(|\gamma_1| - k\gamma_1\right)^a + \left(|\gamma_2| - k\gamma_2\right)^a + \left(|\gamma_3| - k\gamma_3\right)^a \tag{4}$$

and γ_i are:

$$\gamma_1 = \left(\frac{2}{3}L_{11} - \frac{1}{3}L_{12} - \frac{1}{3}L_{14}\right) \tag{5}$$

$$\gamma_2 = \left(\frac{2}{3}L_{12} - \frac{1}{3}L_{22} - \frac{1}{3}L_{24}\right) \tag{6}$$

$$\gamma_3 = \left(\frac{2}{3}L_{14} - \frac{1}{3}L_{24} - \frac{1}{3}L_{44}\right) \tag{7}$$

For a plane stress case, the principal components of equation (3) can be described as follows:

$$\Sigma_1 = \frac{1}{2}\left(\Sigma_{xx} + \Sigma_{yy} + \sqrt{\left(\Sigma_{xx} - \Sigma_{yy}\right)^2 + 4\Sigma_{xy}^2}\right) \tag{8}$$

$$\Sigma_2 = \frac{1}{2}\left(\Sigma_{xx} + \Sigma_{yy} - \sqrt{\left(\Sigma_{xx} - \Sigma_{yy}\right)^2 + 4\Sigma_{xy}^2}\right) \tag{9}$$

$$\Sigma_3 = \Sigma_{zz} \tag{10}$$

where Σ_{xx}, Σ_{yy}, Σ_{xy} and Σ_{zz} are the general components of the modified Cauchy stress tensor explicitly described as:

$$\Sigma_{xx} = \left(\frac{2}{3}L_{11} - \frac{1}{3}L_{12} - \frac{1}{3}L_{14}\right)\sigma_{xx[m]} + \left(-\frac{1}{3}L_{11} + \frac{2}{3}L_{12} - \frac{1}{3}L_{14}\right)\sigma_{yy[m]} \tag{11}$$

$$\Sigma_{yy} = \left(\frac{2}{3}L_{12} - \frac{1}{3}L_{22} - \frac{1}{3}L_{24}\right)\sigma_{xx[m]} + \left(-\frac{1}{3}L_{12} + \frac{2}{3}L_{22} - \frac{1}{3}L_{24}\right)\sigma_{yy[m]} \tag{12}$$

$$\Sigma_{zz} = \left(\frac{2}{3}L_{14} - \frac{1}{3}L_{24} - \frac{1}{3}L_{44}\right)\sigma_{xx[m]} + \left(-\frac{1}{3}L_{14} + \frac{2}{3}L_{24} - \frac{1}{3}L_{44}\right)\sigma_{yy[m]} \tag{13}$$

$$\Sigma_{xy} = L_{33}\sigma_{xy[m]} \tag{14}$$

where $\boldsymbol{\sigma}_{ij[m]}$ are the Cauchy stress components based on the material reference system. Besides, L_{ij} are the anisotropic coefficients related to the texture evolution of the material. The $\boldsymbol{\sigma}_{ij[m]}$ components, described in the tensile test reference system $\boldsymbol{\sigma}_{ij[r]}$ are:

$$\sigma_{xx[m]} = \sigma_{xx[r]}\cos^2\theta + \sigma_{yy[r]}\sin^2\theta + 2\sin\theta\cos\theta\sigma_{xy[r]} \tag{15}$$

$$\sigma_{yy[m]} = \sigma_{xx[r]}\sin^2\theta + \sigma_{yy[r]}\cos^2\theta - 2\sin\theta\cos\theta\sigma_{xy[r]} \tag{16}$$

$$\sigma_{xy[m]} = \left(\sigma_{yy[r]} - \sigma_{xx[r]}\right)\sin\theta\cos\theta + \sigma_{xy[r]}\left(\cos^2\theta - \sin^2\theta\right) \tag{17}$$

It can be demonstrated that for any uniaxial stress state, the yield function (3) can be expressed in terms of:

$$f = \sigma_{\theta^\circ}^a\left[\left(|\Sigma_1| - k\Sigma_1\right)^a + \left(|\Sigma_2| - k\Sigma_2\right)^a + \left(|\Sigma_3| - k\Sigma_3\right)^a\right] = \sigma_{\theta^\circ}^a B_{\theta^\circ} \tag{18}$$

$$\overline{\sigma}_\theta = \left(\frac{B_{0^\circ}}{B_{\theta^\circ}}\right)^{\frac{1}{a}} Y_{\left(\bar{\varepsilon}_p, \dot{\bar{\varepsilon}}_p, T^\circ\right)} \tag{19}$$

where σ_θ^a is the stress applied in the defined direction, and γ are deduced from the previous equations (5)–(7). The subindex θ° denotes the angle referenced to the RD, and a is the degree of homogeneity. Finally, the asymmetry coefficient k is obtained from:

$$k = \frac{1 - \left\{\frac{2^a - 2\left(\frac{\sigma_t}{\sigma_c}\right)^a}{\left(2\frac{\sigma_t}{\sigma_c}\right)^a - 2}\right\}^{\frac{1}{a}}}{1 + \left\{\frac{2^a - 2\left(\frac{\sigma_t}{\sigma_c}\right)^a}{\left(2\frac{\sigma_t}{\sigma_c}\right)^a - 2}\right\}^{\frac{1}{a}}} \tag{20}$$

where (σ_t/σ_c) is the ratio between the yield values at tension and compression over the same direction. Both, σ_t and σ_c are obtained from the uniaxial tensile and compression tests. If the material shows no asymmetry, k is equal to 0. Specifically, for the Zn-20 sheet alloy in this work, symmetric behavior is considered [15].

Based on the equivalent stress definition (2), the Lankford coefficients, considering plastic incompressibility, are defined in the reference frame as:

$$R_{\theta^\circ} = -\frac{\frac{\partial\overline{\sigma}}{\partial\sigma_{yy[r]}}}{\frac{\partial\overline{\sigma}}{\partial\sigma_{xx[r]}} + \frac{\partial\overline{\sigma}}{\partial\sigma_{yy[r]}}} \tag{21}$$

2.3.2. *Hardening function*

The hardening behavior is represented by the Johnson–Cook [30] law written for RD as:

$$Y_{\left(\bar{\varepsilon}_p, \dot{\bar{\varepsilon}}_p, T^\circ\right)} = K\left(\varepsilon_0 + \bar{\varepsilon}_p\right)^n \underbrace{\left[1 + C_1 \ln\left(\frac{\dot{\bar{\varepsilon}}_p}{\dot{\varepsilon}_{ref}}\right)\right]}_{\text{Strain Rate}} \underbrace{\left[1 - \left(\frac{T - T_{ref}}{T_{fusion} - T_{ref}}\right)^{C_2}\right]}_{\text{Temperature-dependent}} \tag{22}$$

Quasi-Static

The function can be divided into quasi-static strain, strain rate, and temperature components. For the quasi-static part, K is the strength coefficient, n is the hardening exponent and $\bar{\varepsilon}_0 = \left(\sigma_{yp}^{RD}/K\right)^{1/n}$, σ_{yp}^{RD} being the yield strength for RD. The rate of the equivalent plastic strain is $\dot{\bar{\varepsilon}}_p = \boldsymbol{\sigma}_{[m]} : \dot{\varepsilon}_p/\overline{\sigma}$, such that $\boldsymbol{\varepsilon}_p$ is the plastic strain tensor with the associated flow rule $\dot{\varepsilon}_p = \dot{\lambda}\partial\overline{\sigma}/\partial\boldsymbol{\sigma}_{[m]}$, where $\dot{\lambda}$ is the plastic consistency parameter. Moreover, in the strain rate component, $\dot{\varepsilon}_{ref}$ is the reference, and lower strain rate (0.002 s^{-1}), $\dot{\varepsilon}$ is the actual strain rate and C_1 is the strain rate coefficient to be fitted.

Lastly, in the temperature component, T_{ref} is the reference temperature, defined to be equal to the lower temperature in tests (20 °C), T_{fusion} is the fusion temperature of the alloy considered as pure zinc (419.5 °C), and T is the actual temperature of the test. Finally, C_2 is the temperature coefficient to be fitted.

2.4. *Model calibration procedure*

The calibration is performed in the plastic range, from the yield point until the Onset of Necking (OS-necking). The yield point is determined based on the Elasticity Modulus defined in 2.1. No variation related to the strain rate or temperature is considered in the elastic range. The fitting procedure is an extension of Alister et al. [15,35].

2.4.1. *Hardening coefficients*

2.4.1.1. *Quasi-static component*. The quasi-static component of equation (21) is the Swift hardening law, resulting from applying the reference strain rate (0.002 s^{-1}) and temperature (20 °C). The Swift coefficients (K, n) were obtained from the minimization of expression (24) based on its explicit form (23) for the two RD experiments at the control condition, i.e., the reference strain rate and temperature; see Table 1.

$$Y_{\left(\bar{\varepsilon}_p\right)} = K\left[\left(\frac{\sigma_{yp}^{RD}}{K}\right)^{\frac{1}{n}} + \bar{\varepsilon}_p\right]^n \tag{23}$$

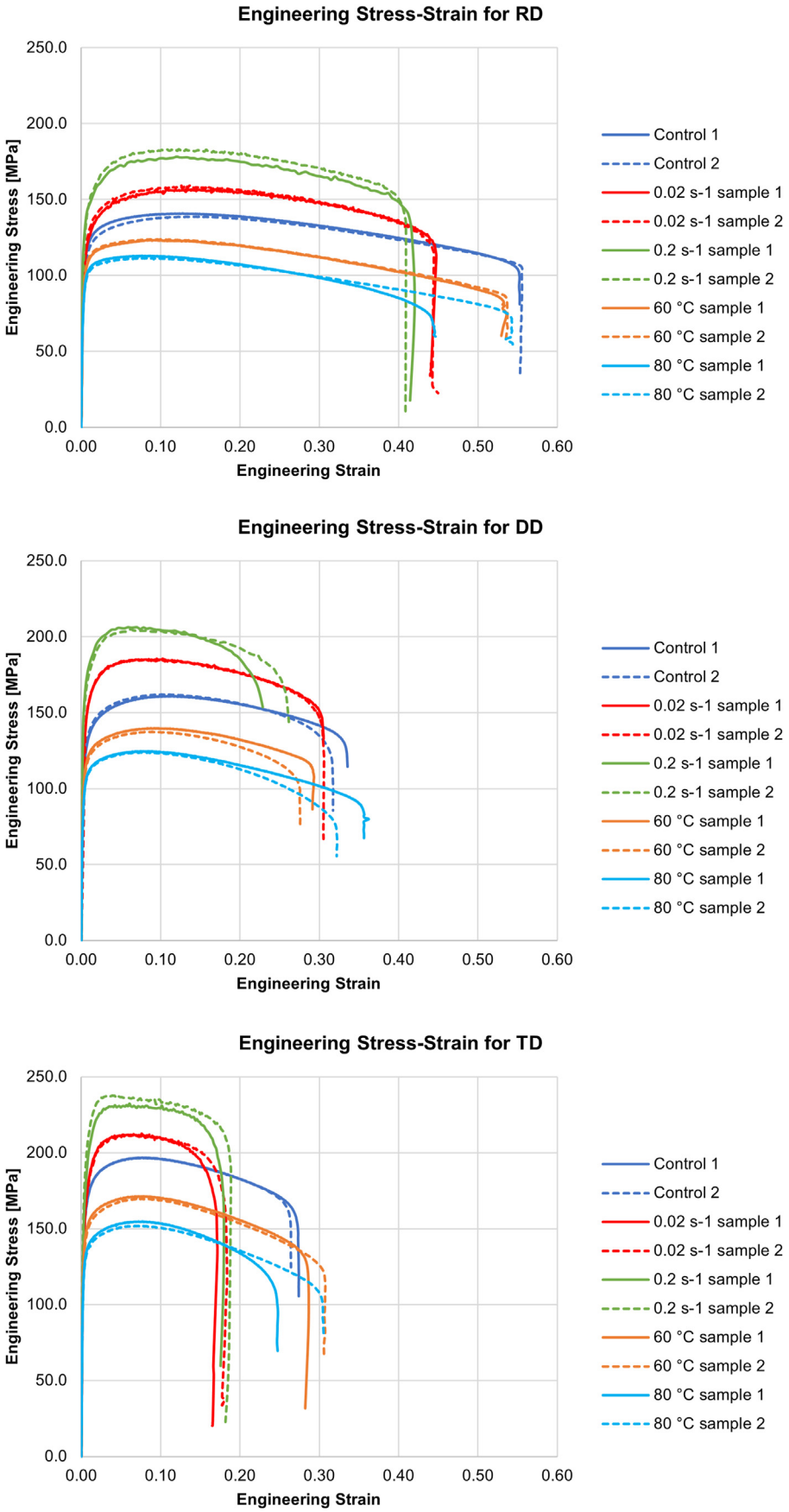

Fig. 2 – Experimental engineering stress–strain curves for all experiments and conditions.

$$\text{Error}_{\dot{\varepsilon}} = \sum_{i=1}^{m} \left(\frac{Y_{(\bar{\varepsilon}_p)}}{\sigma_{RD}^{exp}} - 1 \right)_i^2 \quad (24)$$

were $Y_{(\bar{\varepsilon}_p)}$ is the expression (23) and σ_{RD}^{exp} is the experimentally measured stress values for RD, both experimental and numerical, at the reference strain rate and temperature.

2.4.1.2. *Strain rate component*. The strain rate component is derived from expression (21) at the reference temperature of 20 °C. The coefficient C_1 results from the minimization of expression (26) based on the expression (25) for all the RD experiments at strain rates different from the reference one, i.e., they correspond to values of 0.02 and 0.2 s^{-1} (see Table 1).

$$Y_{(\bar{\varepsilon}_p, \dot{\bar{\varepsilon}}_p)} = K\left(\varepsilon_0 + \bar{\varepsilon}_p\right)^n \left[1 + C_1 \ln\left(\frac{\dot{\bar{\varepsilon}}_p}{\dot{\varepsilon}_{ref}}\right)\right] \quad (25)$$

$$\text{Error}_{\dot{\varepsilon}} = \sum_{i=1}^{m} \left(\frac{Y_{(\bar{\varepsilon}_p, 0.02)}}{\sigma_{0.02}} - 1 \right)_i^2 + \sum_{i=1}^{n} \left(\frac{Y_{(\bar{\varepsilon}_p, 0.2)}}{\sigma_{0.2}} - 1 \right)_i^2 \quad (26)$$

were $Y_{(\bar{\varepsilon}_p, 0.02)}$ and $Y_{(\bar{\varepsilon}_p, 0.2)}$ are expression (25) for strain rates of 0.02 and 0.2, respectively, and $\sigma_{0.02}$ and $\sigma_{0.2}$ are the experimentally measured stress values for each strain rate at the reference temperature.

2.4.1.3. *Temperature component*. The temperature-dependent component is derived from expression (21) at the reference strain rate of 0.002 s^{-1}. Coefficient C_2 results from the minimization of expression (28) using equation (27) for all RD experiments at temperatures different from the reference, i.e., they correspond to values of 60 and 80 °C (see Table 1).

$$Y_{(\bar{\varepsilon}_p, T^\circ)} = K\left(\varepsilon_0 + \bar{\varepsilon}_p\right)^n \left[1 - \left(\frac{T - T_{ref}}{T_{fusion} - T_{ref}}\right)^{C_2}\right] \quad (27)$$

$$\text{Error}_{T^\circ} = \sum_{i=1}^{m} \left(\frac{Y_{(\bar{\varepsilon}_p, 60)}}{\sigma_{60}} - 1 \right)_i^2 + \sum_{i=1}^{n} \left(\frac{Y_{(\bar{\varepsilon}_p, 80)}}{\sigma_{80}} - 1 \right)_i^2 \quad (28)$$

were $Y_{(\bar{\varepsilon}_p, 60)}$ and $Y_{(\bar{\varepsilon}_p, 80)}$ are expression (27) for temperatures of 60 and 80 °C, respectively, and σ_{60} and σ_{80} are the experimentally measured stress values for each temperature at the reference strain rate.

2.4.2. *CPB-06 anisotropy coefficients* L_{ij}

The material parameters of the constitutive model presented are derived through a fitting procedure that only considers the tensile test results. CPB-06 coefficients are obtained using the methodology described in [15,35]. This methodology minimizes the error between the experimental and corresponding analytical values of the tensile true stress–strain curves and Lankford coefficients for three main directions under the different strain and temperature conditions.

$$\begin{aligned} \text{Error}_L = {} & W_{45^\circ}^T \sum_{i=1}^{m} \left(\frac{\sigma_{45^\circ}^{num}}{\sigma_{45^\circ}^{exp}} - 1 \right)_i^2 + W_{90^\circ}^T \sum_{i=1}^{m} \left(\frac{\sigma_{90^\circ}^{num}}{\sigma_{90^\circ}^{exp}} - 1 \right)_i^2 \\ & + W_{0^\circ}^R \sum_{i=1}^{m} \left(\frac{R_{0^\circ}^{num}}{R_{0^\circ}^{exp}} - 1 \right)_i^2 + W_{45^\circ}^R \sum_{i=1}^{m} \left(\frac{R_{45^\circ}^{num}}{R_{45^\circ}^{exp}} - 1 \right)_i^2 \\ & + W_{90^\circ}^R \sum_{i=1}^{m} \left(\frac{R_{90^\circ}^{num}}{R_{90^\circ}^{exp}} - 1 \right)_i^2 \end{aligned} \quad (29)$$

In the present study, L_{11}, L_{55}, and L_{66} were set to 1 [1,3,28,37–41]. Besides, the homogeneity degree a is set to 4, based on the work of Liu et al. [42]. The weights $W_{\theta^\circ}^{T-R}$ were set to 1. In summary, the CPB-06 parameters to be obtained are the remaining six coefficients of tensor L (L_{22}, L_{33}, L_{44}, L_{12}, L_{14} and L_{24}).

The model parameters were fitted in the plastic strain interval ranging from the yield point (σ_{yp}) up to the Onset of Necking over which homogeneous stress and plastic strain field are observed [15,33].

Finally, the accuracy of the fitting procedure is assessed by the Root Mean Square Error (RMSE) between the experimental and corresponding analytical values for both the stress–strain curves and Lankford coefficients through the following expressions:

$$E_\sigma = \sqrt{\frac{1}{m} \sum_{i=1}^{m} \left(\sigma_{\theta^\circ}^{num} - \sigma_{\theta^\circ}^{exp}\right)_i^2} \quad (30)$$

$$E_R = \sqrt{\frac{1}{m} \sum_{i=1}^{m} \left(R_{\theta^\circ}^{num} - R_{\theta^\circ}^{exp}\right)_i^2} \quad (31)$$

3. Results and discussions

The elasto-viscoplastic and the temperature-dependent behavior of Zn-20 alloy has been numerically described by the associated form of the CPB-06 yield function and the Johnson–Cook hardening law. The findings and issues of the applied methodology are presented and discussed below.

3.1. *Experimental results*

3.1.1. *Stress–strain curves*

The studied alloy presents a high anisotropy both in terms of stress–strain curves and Lankford values. The stress–strain curves show that increments in one order of magnitude in strain rate increase the UTS by a mean of 12% without significant changes in the strain value at this point. For example, the UTS strain in RD for the control and medium strain-rate samples is around 0.13 with a stress of 138 MPa and 159.3 MPa, respectively. Although the UTS strain barely changes, the increase in strain rate induces a significant reduction in the final strain in the order of 0.15, 0.10, and 0.18 for RD, DD, and TD, from the control condition to the high strain-rate condition (Fig. 2).

Regarding the temperature dependency, the alloy behavior is opposite to that seen in strain rate, i.e., it means that an increase of temperature induces a softening and an increase of the ultimate strain. Contrary to strain-rate, a reduction in the UTS strain value is also seen in all directions (Fig. 2).

3.1.2. *Lankford coefficients*

Although there is a noticeable change in the stress–strain response under different strain rates or temperatures, the Lankford coefficients (R-value) show no significant difference in their evolution. As can be seen in Fig. 3, R-value did not change their trends during the test. Consequently, RD presents a slight increase while DD has an enduring value. Finally, TD shows a steady reduction in the R-value from the

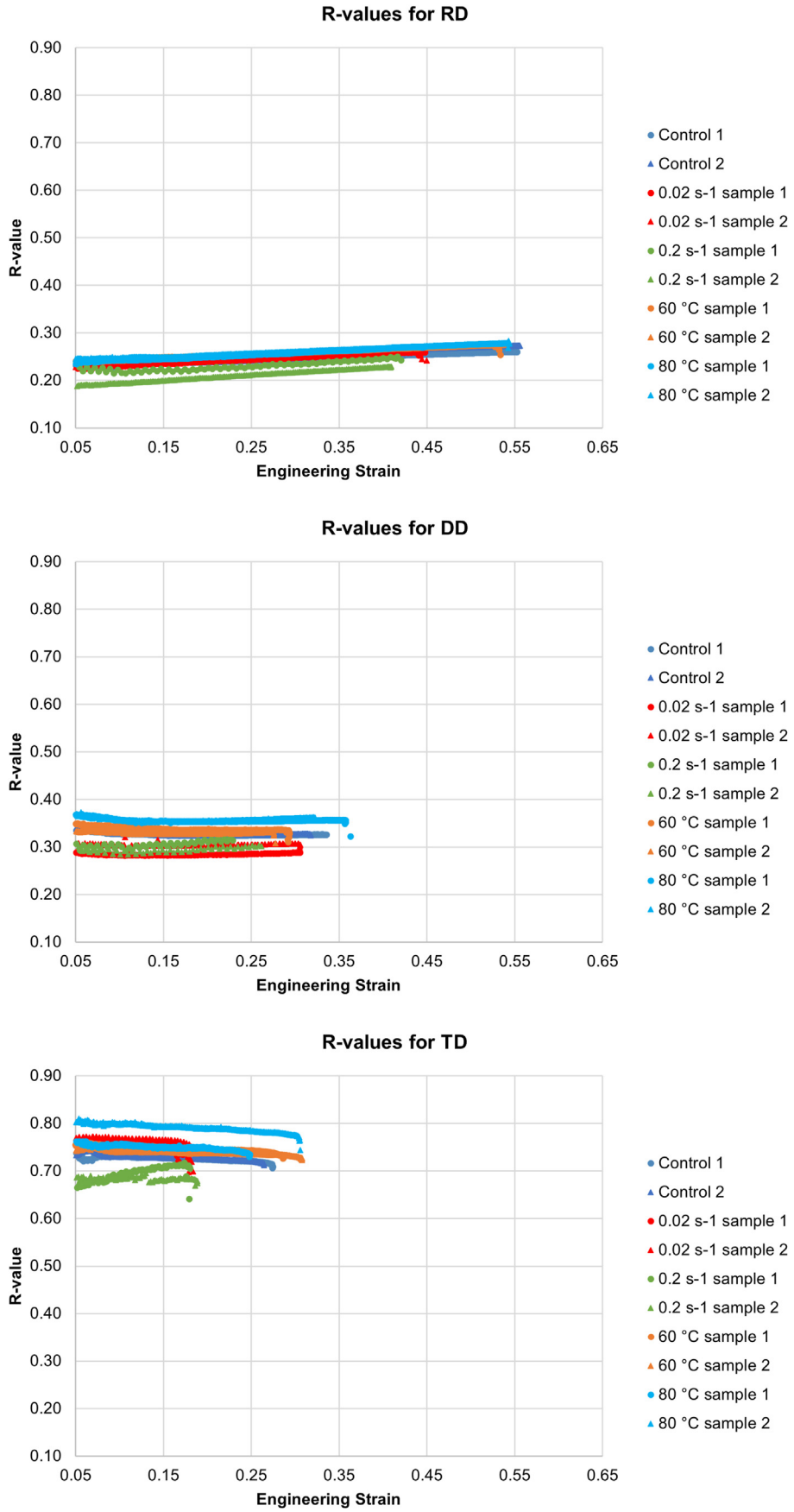

Fig. 3 – Experimental Lankford coefficient vs. engineering strain curves for all experiments and conditions.

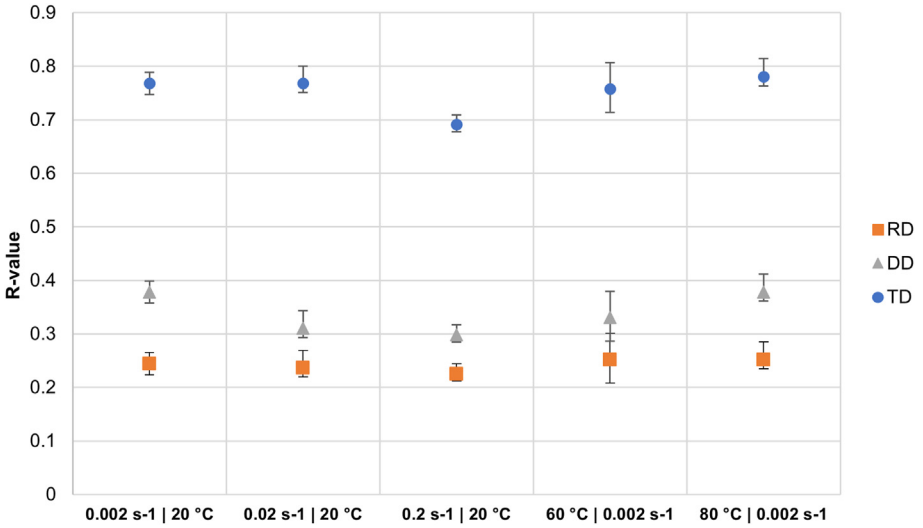

Fig. 4 – Dispersion around the mean R-value for all experiments and conditions.

Table 2 – Johnson–Cook fitted coefficients.

K (MPa)	ε_0	n	C_1	C_2
197.2	0.004	0.105	0.0615	0.9680

beginning until the end of the tests. No matter what the conditions were, the trend is the same for the same direction.

Figure 4 presents the registered R-value, from yield to OS Necking, averaged for two repetitions in the same condition and direction. Besides, the dispersion bars are also represented. The plot shows no significant difference between the control case (0.002 s^{-1} at 20 °C) and the temperature and strain rate cases for all conditions and directions.

In general, there is a slight increment of the R-value at high temperatures (80 °C) for all directions, especially for DD. On the other hand, the high strain rate condition (0.2 s^{-1}) decreases the mean R-value for all directions. RD's maximum and minimum R-value are 0.23 and 0.25, respectively, in terms of specifics values. For DD, 0.38 and 0.30 while for TD are 0.78 and 0.80. The maximum and minimum mean R-value correspond to the high-temperature case (80 °C) and high strain rate (0.2 s^{-1}), respectively. However, based on the data scattering, it is not possible to establish a correlation in the alloy's response to the strain rate or temperature.

Even when the stress–strain curves presented in Fig. 2 show a clear difference for a specific direction in the different conditions, the R-value is almost constant. Fig. 4 shows that there is no trend between the experimental condition and Lankford coefficients for all directions. Thus, the R-value can be considered independent of strain rate (0.002, 0.02, and 0.2 s^{-1}), temperature (20, 60, and 89 C°), and constants for the plastic range from yield to the OS-necking.

3.2. *Numerical results*

3.2.1. *Fitted material model parameters*

Based on the previous statement, it is possible to use a unique set of anisotropy L coefficients (see 2.3.1) to describe the stress and plastic behavior of the alloy. Therefore, the hardening law's definition is driven only by RD in all strain-rate and temperature conditions, while the CPB-06 yield function adapts the hardening curves to the other directions. On the other hand, the Lankford coefficients are fitted for all directions and conditions.

As was set before, no asymmetry is considered; thus, k is equal to 0. The degree of homogeneity (parameter a) was fixed to 4, based on a previous trial test [15,35]. In addition, the experimental findings of Liu [42] and Nurcheshmeh [43] show a better approximation with fourth-order yield models for some HCP materials.

The obtained Johnson–Cook and CPB-06 fitted coefficients are respectively presented in Tables 2 and 3.

3.2.2. *Stress–strain curves*

The result of the fitting process is applied and shown in Fig. 5 for stress–strain curves. For all conditions, RD is the best reproduced for all combinations. However, in all directions, the alloy's softening by increasing temperature is not well represented. The adjusted true stress–strain curves for the RD, DD, and TD directions in all conditions are presented in Fig. 5. Here, the range of interest is bounded from the yield until the OS-Necking strain.

Table 3 – CPB-06 fitted coefficients.

L_{11}	L_{12}	L_{14}	L_{22}	L_{24}	L_{33}	L_{44}	k	a
1.000	0.055	−0.191	0.853	0.025	0.856	1.056	0.0	4.0

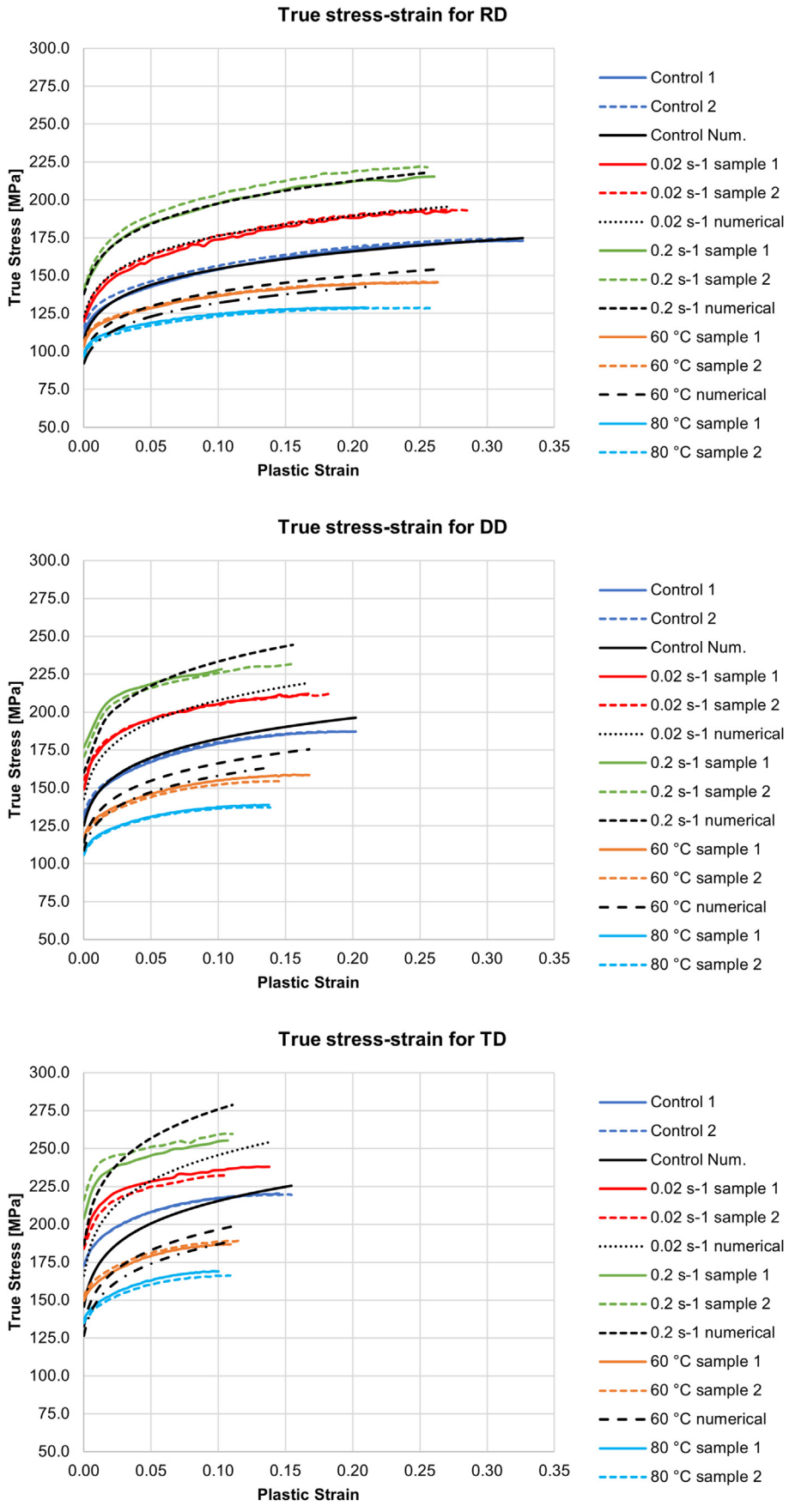

Fig. 5 – Experimental and numerical true stress–strain plots all directions and conditions. From top to bottom: RD, DD, and TD, respectively.

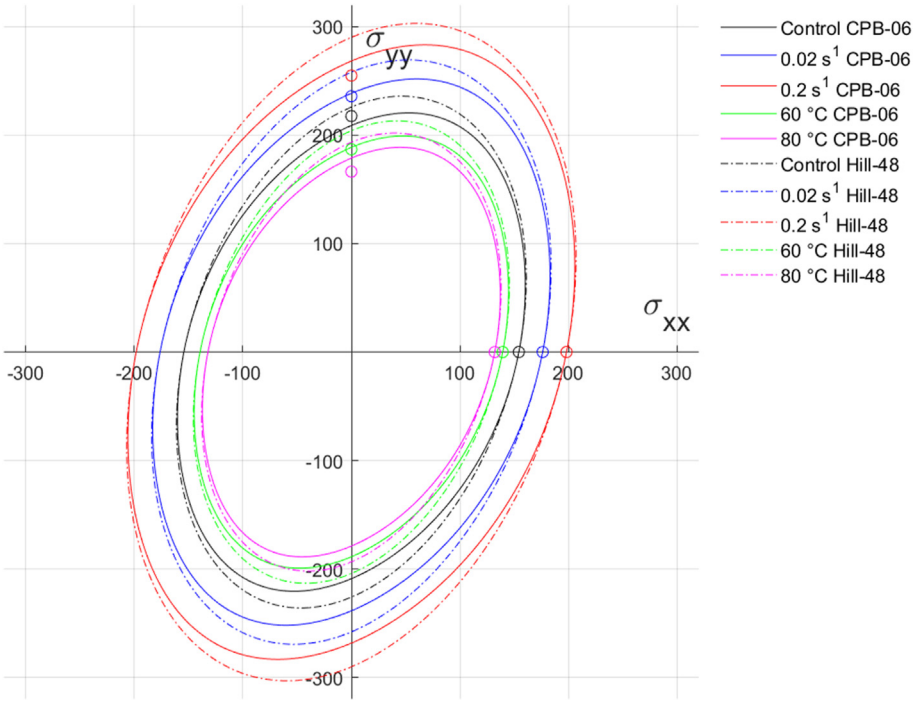

Fig. 6 – Yield loci for all conditions at 0.10 of plastic strain for $\sigma_{xy} = 0$. Circles indicate the experimental yield value for both RD and TD in the respective condition (black: control, blue: medium strain, red: high strain, green: medium-temperature, and magenta: high temperature).

The plot of the yield loci at 0.1 of plastic strain for all conditions in Fig. 6 shows the constitutive model's ability to describe the alloy's anisotropy based on a unique set of anisotropy coefficients (L_{ij}). Simultaneously, the underestimation of the yield value for TD is seen for each condition. However, the approach by CPB-06 is always better than Hill-48. The evolution of the alloy asymmetry related to the strain rate and temperature should be studied. The shape of the yield loci suggests that modifying the asymmetry coefficient "k" could improve the yield point determination for TD. The use of the non-quadratic yield function, as suggested by Liu [42] and Nurcheshmeh [43], gives good results for this material.

The yield loci for a plastic strain of 0.10 and the different experiments are plotted in Fig. 6 for $\sigma_{xy} = 0$. The different approximation of CPB-06 based on the same set of anisotropy coefficients compared to Hill-48 based on R-value [44] can be seen. The colored circles denote the experimental yield values for RD and TD.

3.2.3. *Lankford coefficients*

The result of the fitting process is applied and shown in Fig. 7 for R-value. In general, the analytically reproduced values show a good approximation for all directions, and it can be considered a means of all conditions. A limitation of the proposed methodology is the constant value of the anisotropy coefficients. In this sense, Plunkett and Wu [45,46] proposed an evolution scheme of the anisotropy coefficients as a function of the cumulative plastic strain. Besides, the same structure could be considered for asymmetry evolution. This change in the methodology could improve the match of the analytical curves, especially for TD in the high strain rate condition and all directions in the high-temperature scenario.

The adjusted true Lankford curves for RD, DD, and TD directions in all conditions are presented in Fig. 7, where the R-value is plotted against the axial plastic strain. The range of interest is bounded from 0.1 of plastic strain until the OS-Necking, avoiding R-value's initial noise. Because there is no dependency of the R-value to the test conditions, only the numerical control is plotted to avoid redundancy.

3.2.4. *RMSE results*

The RMSE is graphically presented in Figs. 8 and 9 for each direction and condition. The results are based on the functions presented in equations (29) and (30) for stress and R-value. Fig. 8 shows the numerical RMSE for the stress–strain curves.

The worst approaches are the high strain rate condition followed by the high temperature for all directions and repetitions. In DD and TD, which have the highest RMSE value, the strain rate is by far the less precise modeled condition. The best approaches are obtained for all directions in the control case (0.002 s^{-1} at °C).

In comparison, for the TD case, the strain rate condition almost doubles the high-temperature RMSE. Then, it would be interesting to study the evolution of anisotropy coefficients as a function of strain rate or accumulated plastic strain.

In general, for stress–strain curves, the RMSE tends to be constant for all directions and cases, with an RMSE close to

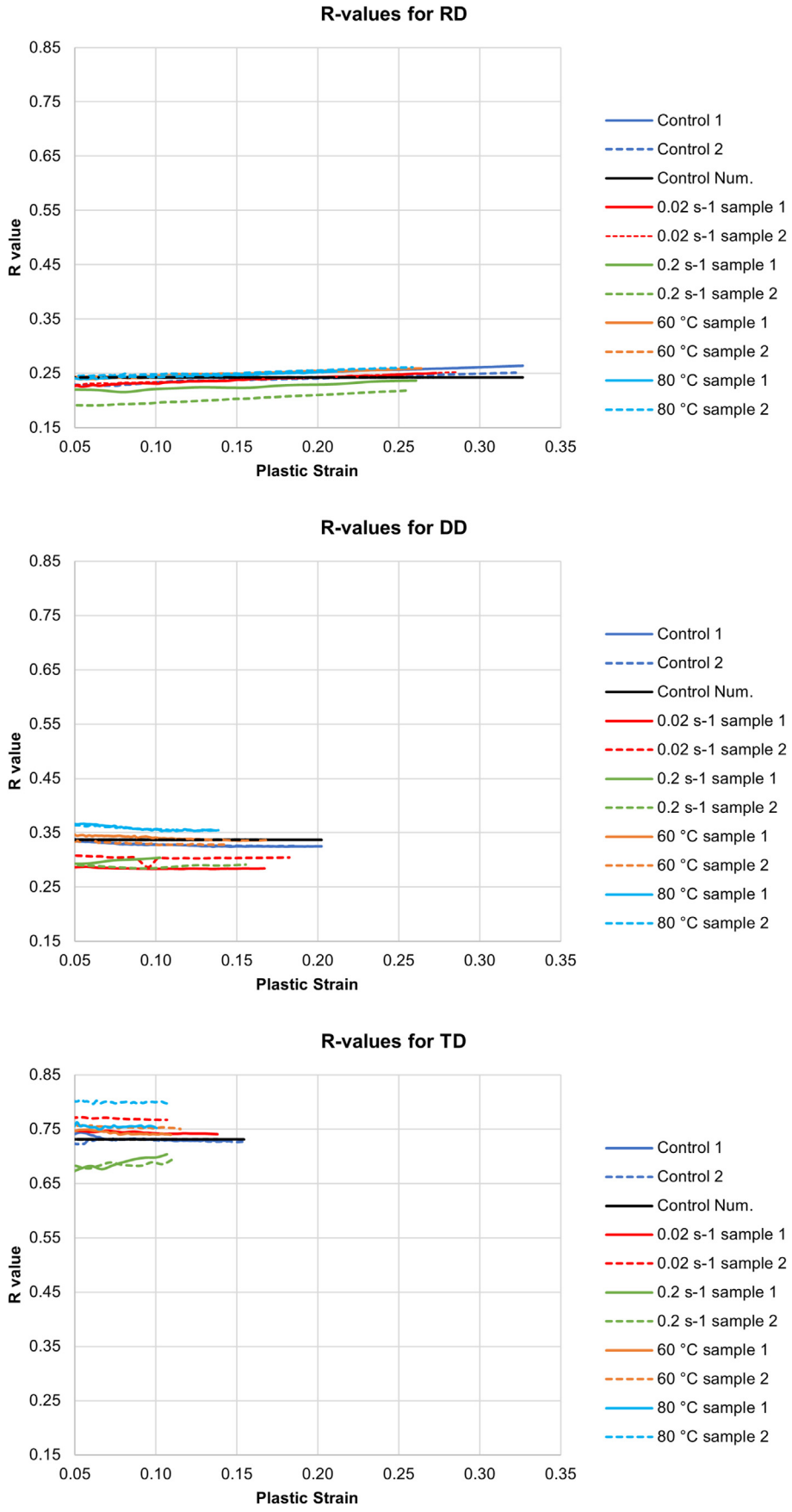

Fig. 7 – Experimental and numerical Lankford coefficient vs. plastic strain curves for all directions and conditions. From top to bottom: RD, DD, and TD, respectively.

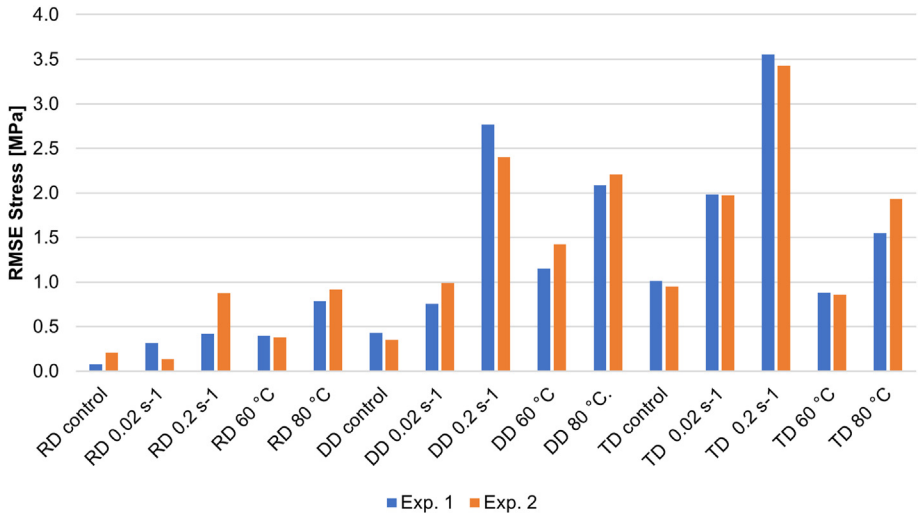

Fig. 8 – True stress RMSE for each direction, condition, and repetition based on the numerical model.

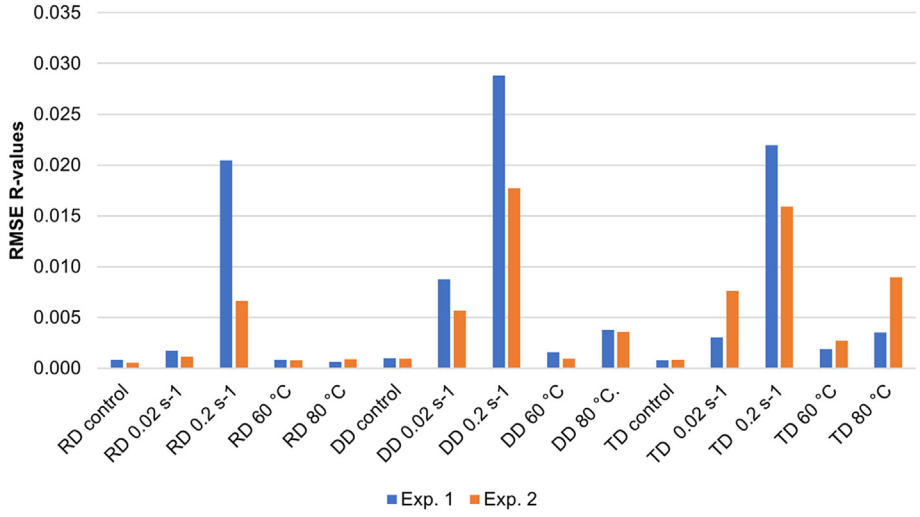

Fig. 9 – Lankford coefficient RMSE for each direction, condition, and repetition based on the numerical model.

1.0 MPa, except for DD, TD, high strain rates, and high-temperature conditions where the value surpasses 2.0 MPa.

Fig. 9 shows the numerical RMSE for the Lankford curves for each experiment and condition.

For R-value, the less precise approaches are for the high strain and high-temperature conditions for all directions, while the best results are obtained for the control condition. In contrast with the stress RMSE, the high strain rate values are more significant than the other conditions. In this sense, for all other conditions, the RMSE is around 0.05.

4. Conclusions

The Zn-20 alloy exhibits a complex behavior for hardening and R-value. Moreover, the response of the material is highly influenced by the strain rate and temperature. A constitutive model based on CPB-06/Johnson–Cook is implemented to replicate the experimental uniaxial test results through an associated elasto-viscoplastic model.

The experimental results show that R-value is not significantly affected while the strain rate and temperature highly influence hardening. Therefore, the fitting process was performed for base or control conditions while the hardening law, together with anisotropy coefficients, broadly describes the material behavior for other scenarios.

The use of CPB-06/Johnson–Cook in its associated form, and the proposed fitting procedure, are fast and straightforward, demonstrating that it can deal with the complex behavior of Zn-20 without compromising the accuracy of the results. This work is presented as a base framework to drive numerical simulation dedicated to industrial forming process.

Improvements need to be performed to achieve better agreements for directions different from RD, especially TD. In this sense, evolving anisotropy coefficients or exploring the alloy's asymmetry behavior are presented as a new challenge in this research.

Contribution of authors

F. Alister: experimental tests, software programing, analysis of results, writing – original draft.

D. Celentano: Supervision, software programing, analysis of results, writing – original draft, funding acquisition.

J. Signorelli: Supervision, writing – review & editing.

P-O. Bouchard: Supervision, writing – review & editing, Funding acquisition.

D. Pino: writing – review & editing.

M. Cruchaga: writing – review & editing.

Funding

This work has been supported by the funds provided by the "Comisión Nacional de Investigación Científica y Tecnológica" CONICYT-Chile, through the ECOS-SUD Chile project C16E02 and the Fondecyt Project 1180591.

Declaration of Competing Interest

The authors declare no conflict of interest.

Acknowledgments

Javier Signorelli thanks the Pontificia Universidad Católica de Chile for the program "Fortalecimiento de Redes de Colaboración Académica Internacional". Francisco Alister thanks the Comisión Nacional de Investigación Científica y Tecnologíca CONICYT-CHILE by its support through the doctoral scholarship CONICYT-PCHA/Doctorado Nacional/2015-21150598. The experimental campaign was performed by the close collaboration of the Centre de Mise en Forme des Materiaux (CEMEF, France). All the material was provided by VM Zinc (Auby, France).

REFERENCES

[1] Revil-Baudard B, Chandola N, Cazacu O, Barlat F. Correlation between swift effects and tension-compression asymmetry in various polycrystalline materials. J Mech Phys Solid 2014;70:104–15. https://doi.org/10.1016/j.jmps.2014.05.012.

[2] Gilles G, Hammami W, Libertiaux V, Cazacu O, Yoon JH, Kuwabara T, et al. Experimental characterization and elasto-plastic modeling of the quasi-static mechanical response of TA-6 v at room temperature. Int J Solid Struct 2011;48:1277–89. https://doi.org/10.1016/j.ijsolstr.2011.01.011.

[3] Chandola N, Lebensohn RA, Cazacu O, Revil-Baudard B, Mishra RK, Barlat F. Combined effects of anisotropy and tension-compression asymmetry on the torsional response of AZ31 Mg. Int J Solid Struct 2015;58:190–200. https://doi.org/10.1016/j.ijsolstr.2015.01.001.

[4] Barros PD, Alves JL, Oliveira MC, Menezes LF. Modeling of tension-compression asymmetry and orthotropy on metallic materials: numerical implementation and validation. Int J Mech Sci 2016;114:217–32. https://doi.org/10.1016/j.ijmecsci.2016.05.020.

[5] Kakogiannis D, Verleysen P, Belkassem B, Coghe F, Rabet L. Multiscale modelling of the response of Ti-6AI-4V sheets under explosive loading. Int J Impact Eng 2018;119:1–13. https://doi.org/10.1016/j.ijimpeng.2018.04.008.

[6] Williams BW, Boyle K. Characterization of anisotropic yield surfaces for titanium sheet using hydrostatic bulging with elliptical dies. Int J Mech Sci 2016;114:315–29. https://doi.org/10.1016/j.ijmecsci.2016.05.022.

[7] Kabirian F, Khan AS. Anisotropic yield criteria in T-S Stress space for materials with yield asymmetry. Int J Solid Struct 2015;67(68):116–26. https://doi.org/10.1016/j.ijsolstr.2015.04.006.

[8] Diot M, Fundenberger JJ, Philippe MJ, Wegria J, Esling C. Texture gradient in rolled zinc sheets. Scr Mater 1998;39:1623–30. https://doi.org/10.1016/S1359-6462(98)00363-7.

[9] Philippe MJ, Wagner F, Mellab C, Esling C, Wegria J. Modelling of texture evolution for materials of hexagonal symmetry – I. Application to zinc alloys. Acta Metall Mater 1994;42:239–50.

[10] Fundenberger JJ, Philippe MJ, Wagner F, Esling C. Modelling and prediction of mechanical properties for materials with hexagonal symmetry (zinc, titanium and zirconium alloys). Acta Mater 1997;45:4041–55. https://doi.org/10.1016/S1359-6454(97)00099-2.

[11] Philippe MJ, Fundenberger JJ, Galledou Y, Humbert M, Wegria J, Esling C. Influence of texture on low temperature bendability of Zn alloys. Textures Microstruct 1991;14:471–6. https://doi.org/10.1155/TSM.14-18.471.

[12] Faur M, Cosmeleaţă G. Effects of hot and cold rolling on the microstructure of low alloy Zn-Cu and Zn-Cu-Ti zinc alloy with improved corrosion resistance. UPB Sci Bull Ser B Chem Mater Sci 2006;68:67–74.

[13] Pantazopoulos G, Toulfatzis A, Vazdirvanidis A, Rikos A. Fundamental aspects of rolled Zn alloy sheet formability: structure-property and failure mode relationships. Mater Sci Forum 2017;879:1443–8. https://doi.org/10.4028/www.scientific.net/MSF.879.1443.

[14] Milesi M, Logé R, Pino D, Jansen Y, Bouchard P-O. Accounting for material parameters scattering in rolled zinc formability. J Mater Process Technol 2017;245:134–48. https://doi.org/10.1016/j.jmatprotec.2017.02.021.

[15] Alister F, Celentano D, Nicoletti E, Signorelli J, Bouchard P-O, Pino D, et al. Elastoplastic characterization of Zn-Cu-Ti alloy sheets: experiments, modeling and simulation. J Mater Eng Perform 2021. https://doi.org/10.1007/s11665-021-06226-w.

[16] Schlosser F, Signorelli J, Leonard M, Roatta A, Milesi M, Bozzolo N. Influence of the strain path changes on the formability of a zinc sheet. J Mater Process Technol 2019;271:101–10. https://doi.org/10.1016/j.jmatprotec.2019.03.026.

[17] Cauvin L, Raghavan B, Bouvier S, Wang X, Meraghni F. Multi-scale investigation of highly anisotropic zinc alloys using crystal plasticity and inverse analysis. Mater Sci Eng A 2018;729:106–18. https://doi.org/10.1016/j.msea.2018.05.038.

[18] Schwindt C. Desarrollo experimental y modelado computacional multiescala de la curva limite de formabilidad. Aplicacion a un acero Dual-Phase de alta resistencia. Universidad de Rosario; 2015.

[19] Borodachenkova M, Wen W, Barlat F, Pereira A, Grácio J. Modeling of the mechanical behavior and texture evolution in Zn alloys during reverse shear loading. J Mater Process Technol 2015;224:143–8. https://doi.org/10.1016/j.jmatprotec.2015.04.021.

[20] Jansen Y, Logé R, Manach P-Y, Carbuccia G, Milesi M. On the benefits of a stress criterion for the simulation of cup drawing process. Int J Mater Form 2016. https://doi.org/10.1007/s12289-016-1313-8.

[21] Jansen Y, Logé R, Milesi M, Manov S, Massoni E. Theoretical and experimental evaluation of the formability of anisotropic zinc sheets. Key Eng Mater 2011;473:390–5. https://doi.org/10.4028/www.scientific.net/KEM.473.390.
[22] Jansen Y, Logé R, Milesi M, Manov S, Massoni E. Using cross stamping to test zinc sheets formability. Key Eng Mater 2012;504–506:65–70. https://doi.org/10.4028/www.scientific.net/KEM.504-506.65.
[23] Jansen Y, Logé R, Milesi M, Massoni E. An anisotropic stress based criterion to predict the formability and the fracture mechanism of textured zinc sheets. J Mater Process Technol 2013;213:851–5. https://doi.org/10.1016/j.jmatprotec.2012.12.006.
[24] Milesi M, Logé R, Jansen Y. Anisotropic mechanical behavior and formability criterion for zinc sheets. J Mater Process Technol 2014;214:2869–76. https://doi.org/10.1016/j.jmatprotec.2014.06.023.
[25] Milesi M, Chastel Y, Hachem E, Bernacki M, Logé R, Bouchard P-O. A multi-scale approach for high cycle anisotropic fatigue resistance: application to forged components. Mater Sci Eng A 2010;527:4654–63. https://doi.org/10.1016/j.msea.2010.03.042.
[26] Milesi M, Lecoq J, Pradille C, Vitu L, Boudeau N, Bouchard P-O. Impact of strain rate sensitivity on the identification of the material parameters scattering and on the formability of zinc sheet. Int J Mater Form 2020;13:203–18. https://doi.org/10.1007/s12289-019-01479-2.
[27] Milesi M, Pino D, Lagroum A, Pradille C, Bouchard P-O. Self-heating of rolled ZnCuTi sheets. Sadhana – Acad Proc Eng Sci 2020;45:1–11. https://doi.org/10.1007/s12046-020-01426-x.
[28] Cazacu O, Plunkett B, Barlat F. Orthotropic yield criterion for hexagonal closed packed metals. Int J Plast 2006;22:1171–94. https://doi.org/10.1016/j.ijplas.2005.06.001.
[29] Plunkett B, Cazacu O, Barlat F. Orthotropic yield criteria for description of the anisotropy in tension and compression of sheet metals. Int J Plast 2008;24:847–66. https://doi.org/10.1016/j.ijplas.2007.07.013.
[30] Johnson GR, Cook WH. A constitutive model and data for metals subjected to large strains, high strain rates and high temperatures. In: 7th international symposium on ballistics; 1983. p. 541–7. https://doi.org/10.1038/nrm3209.
[31] Ledbetter HM. Elastic properties of zinc: a compilation and a review. J Phys Chem Ref Data 1977;6:1181–203. https://doi.org/10.1063/1.555564.
[32] Tromans D. Elastic anisotropy of HCP metal crystals and polycrystals. Int J Res Rev Appl Sci 2011;6:462–83.
[33] Leonard M, Nicoletti E, Roatta A, Stout M, Bolmaro R, Signorelli J. Study of zinc-sheet mechanical anisotropy and its relationship to crystallographic texture. Rev Latinoam Metal Mater 2019;8:43–7.
[34] Plunkett B, Lebensohn RA, Cazacu O, Barlat F. Anisotropic yield function of hexagonal materials taking into account texture development and anisotropic hardening. Acta Mater 2006;54:4159–69. https://doi.org/10.1016/j.actamat.2006.05.009.
[35] Alister F, Celentano D, Signorelli J, Bouchard P-O, Pino D, Cruchaga M. Characterization of the elastoplastic response of low zn-cu-ti alloy sheets using the CPB-06 criterion. Materials 2019;12. https://doi.org/10.3390/ma12193072.
[36] Celentano D, Guelorget B, Francois M, Cruchaga M, Slimane A. Numerical simulation and experimental validation of the microindentation test applied to bulk elastoplastic materials. Model Simul Mater Sci Eng 2012:196–8. https://doi.org/10.1088/0965-0393/20/4/045007.
[37] Cazacu O, Ionescu IR, Yoon JW. Orthotropic strain rate potential for the description of anisotropy in tension and compression of metals. Int J Plast 2010;26:887–904. https://doi.org/10.1016/j.ijplas.2009.11.005.
[38] Yoon JH, Cazacu O, Mishra RK. Constitutive modeling of AZ31 sheet alloy with application to axial crushing. Mater Sci Eng A 2013;565:203–12. https://doi.org/10.1016/j.msea.2012.12.054.
[39] Tuninetti V, Gilles G, Péron-lührs V, Habraken AM. Compression test for metal characterization using digital image correlation and inverse modeling. Procedia IUTAM 2012;4:206–14. https://doi.org/10.1016/j.piutam.2012.05.022.
[40] Tuninetti V, Gilles G, Milis O, Pardoen T, Habraken AM. Anisotropy and tension-compression asymmetry modeling of the room temperature plastic response of Ti-6Al-4V. Int J Plast 2015;67:53–68. https://doi.org/10.1016/j.ijplas.2014.10.003.
[41] Muhammad W, Mohammadi M, Kang J, Mishra RK, Inal K. An elasto-plastic constitutive model for evolving asymmetric/anisotropic hardening behavior of AZ31B and ZEK100 magnesium alloy sheets considering monotonic and reverse loading paths. Int J Plast 2015;70:30–59. https://doi.org/10.1016/j.ijplas.2015.03.004.
[42] Liu C, Huang Y, Stout MG. On the asymmetric yield surface of plastically orthotropic materials: a phenomenological study. Acta Mater 1997;45:2397–406. https://doi.org/10.1016/S1359-6454(96)00349-7.
[43] Nurcheshmeh M, Green DE. Prediction of forming limit curves for nonlinear loading paths using quadratic and non-quadratic yield criteria and variable imperfection factor. Mater Des 2016;91:248–55. https://doi.org/10.1016/j.matdes.2015.11.098.
[44] Hill R. A theory of the yielding and plastic flow of anisotropic metals. Proc R Soc A Math Phys Eng Sci 1948;260:459–74.
[45] Plunkett B, Cazacu O, Lebensohn RA, Barlat F. Elastic-viscoplastic anisotropic modeling of textured metals and validation using the Taylor cylinder impact test. Int J Plast 2007;23:1001–21. https://doi.org/10.1016/j.ijplas.2006.10.008.
[46] Wu S-H, Song N-N, Pires F, Santos A. Prediction of forming limit diagrams for materials with HCP structure. Acta Metall Sin 2015;28:1–10. https://doi.org/10.1007/s40195-015-0344-3.